Geomorphology 250 (2015) 1–14

Contents lists available at ScienceDirect

Geomorphology

journal homepage: www.elsevier.com/locate/geomorph

Subsurface flow in a soil-mantled subtropical dolomite karst slope: A field rainfall simulation study

Z.Y. Fu [a,b], H.S. Chen [a,b,*], W. Zhang [a,b], Q.X. Xu [a,d], S. Wang [a,b,c], K.L. Wang [a,b]

[a] Key Laboratory of Agro-ecological Processes in Subtropical Region, Institute of Subtropical Agriculture, Chinese Academy of Sciences, Changsha, Hunan 410125, China
[b] Huanjiang Observation and Research Station for Karst Ecosystems, Chinese Academy of Sciences, Huanjiang, Guangxi 547100, China
[c] Graduate University of Chinese Academy of Sciences, Beijing 100049, China
[d] College of Environmental Science and Engineering, Guilin University of Technology, Guilin 541004, China

ARTICLE INFO

Article history:
Received 23 January 2015
Received in revised form 28 July 2015
Accepted 18 August 2015
Available online 22 August 2015

Keywords:
Karst
Subsurface flow
Rainfall simulation
Irregular bedrock
Soil–epikarst interface

ABSTRACT

Soil and epikarst co-evolve resulting in complex structures, but their coupled structural effects on hydrological processes are poorly understood in karst regions. This study examined the plot-scale subsurface flow characteristics from an integrated soil–epikarst system perspective in a humid subtropical cockpit karst region of Southwest China. A trench was excavated to the epikarst lower boundary for collecting individual subsurface flows in five sections with different soil thicknesses. Four field rainfall simulation experiments were carried out under different initial moisture conditions (dry and wet) and rainfall intensities (114 mm h^{-1} (high) and 46 mm h^{-1} (low) on average). The soil–epikarst system was characterized by shallow soil overlaying a highly irregular epikarst surface with a near-steady infiltration rate of about 35 mm h^{-1}. The subsurface flows occurred mainly along the soil–epikarst interface and were dominated by preferential flow. The subsurface flow hydrographs showed strong spatial variability and had high steady-state coefficients (0.52 and 0.36 for high and low rainfall intensity events). Irregular epikarst surface combining with high vertical drainage capacity resulted in high threshold rainfall depths for subsurface flows: 67 mm and 263 mm for initial wet and dry conditions, respectively. The above results evidenced that the irregular and permeable soil–epikarst interface was a crucial component of soil–epikarst architecture and consequently should be taken into account in the hydrological modeling for karst regions.

1. Introduction

In karst regions, soil and epikarst co-evolve during karstification (Klimchouk, 2004; Williams, 2008). The soil–epikarst system is the foundation for the vadose critical zone of epigenic karst (Schwartz et al., 2013). It is a complex network of soil pockets, rock matrix, and flow paths of variable hydraulic conductivity (Estrada-Medina et al., 2013). This architecture is structurally different from the regoliths of non-karst areas which exhibit weathered non-soluble bedrock horizons beneath soils. Soil–epikarst architecture determines various near-surface hydrological processes in a karst system just as soil architecture dictates various flow pathways and soil water distribution patterns in the soil (Lin et al., 2005; Lin, 2010; Zhang et al., 2011). These karst-area, near-surface hydrological processes have received considerable attention, mainly due to their important roles in: 1) soil erosion (Cerdà, 1998d; Feng et al., 2014); 2) groundwater recharge (Wilcox et al., 2008; Jiang et al., 2015); 3) karst land degradation (Bai et al., 2013; Xu and Zhang, 2014; Yan and Cai, 2015); and 4) vegetation restoration (Nie et al., 2014).

Since the 1990s, surface hydrological processes of karst hillslopes have mainly been investigated in semi-arid and arid areas (Cerdà, 1997c, 1998d; Li et al., 2011). As a widespread methodology for measuring the runoff and soil erosion in different ecosystems (Iserloh et al., 2012, 2013; Martínez-Murillo et al., 2013; Ziadat and Taimeh, 2013; Moreno-Ramón et al., 2014), rainfall simulation was frequently used in their studies. These findings clarified the infiltration–runoff regulatory roles played by climate (Cerdà, 1997a, 1998a, 1998b), parent material (Cerdà, 1999), soil surface components (such as vegetation, rock outcrop, fracture, rock fragment, and soil crust) (Cerdà, 1997c, 1998c, 2001), topographic position (Cerdà, 1998d; Calvo-Cases et al., 2003), antecedent soil moisture (Li et al., 2011), and land abandonment (Cerdà, 1997b). The Hortonian discontinuous runoff model and the mixed infiltration and saturation excess runoff generation model have been the two major runoff-generation conceptual models for Mediterranean karst areas (Cerdà, 1998d; Calvo-Cases et al., 2003; Lange et al., 2003).

More recently, recognizing that karst landscapes are typically rich in solution features and the overlying shallow soil is highly permeable,

* Corresponding author at: Institute of Subtropical Agriculture, Chinese Academy of Sciences, No. 644, Yuanda 2nd Road, Changsha, Hunan 410125, China.
E-mail addresses: zyfu@isa.ac.cn (Z.Y. Fu), hbchs@isa.ac.cn (H.S. Chen), zhangw@isa.ac.cn (W. Zhang), xqx@glut.edu.cn (Q.X. Xu), hjdx@foxmail.com (S. Wang), kelin@isa.ac.cn (K.L. Wang).

http://dx.doi.org/10.1016/j.geomorph.2015.08.012
0169-555X/

many researchers have focused on the roles played by underground properties (especially the epikarst architecture) on subsurface flow through sub-humid and semi-arid karst hillslopes using a number of different methods: (1) trench investigation (Wilcox et al., 2008); (2) dye-tracer testing (Nobles et al., 2010); (3) time-domain reflectometry (TDR) (Dasgupta et al., 2006); and (4) ground penetrating radar (GPR) and electrical resistance (Leh et al., 2008). For example, Wilcox et al. (2007) described a unique soil–epikarst architecture formed in a sequence of limestone and dolomite beds in the Texas Hill Country. In this unique architecture; water flow from uplands to valley floors was a combination of surface and subsurface flow conducted through a series of cascading recharge/discharge microtopographic units (Nobles et al., 2010). After that, by conducting rainfall simulation experiments on trenched plots within the Edwards Aquifer region, Wilcox et al. (2008) again demonstrated the importance of subsurface flow in semi-arid karst shrub lands, revealing that the differences in surface runoff and subsurface flow could be attributed to vegetation and epikarstic differences. On a Savoy karst hillslope, Leh et al. (2008) found that hillslope fractures acted as reservoirs which, when filled up, could impede infiltration excess surface flow while facilitating saturated subsurface flow. They also suggested that it was essential to know sub-surface fractures, joints, bedding planes and distinctive soil horizons locations in order to understand the three-dimensional details of flow pathways that control runoff processes in karst regions. In a shallow epikarst, Dasgupta et al. (2006) observed from a trenched plot that subsurface flow occurred as a combination of preferential flow and matrix flow. Most of the flow moved rapidly through open limestone conduits and fractures and root channels, with a smaller amount moving through narrower fractures. The least amount of subsurface flow was through soil matrix. Preferential flow at the trench face depended on total rainfall and was independent of antecedent soil matrix moisture levels (Dasgupta et al., 2006). The subsurface flow pathways in shallow epikarst usually display great variability and a high level of interconnectedness (Taucer et al., 2005).

An integrated soil–epikarst system extends down from the soil surface to the epikarst base (Schwartz et al., 2013). Soil and epikarst coevolution leads to a highly connected preferential flow pathway network embedded throughout a soil–epikarst system (Klimchouk, 2004). A complete understanding of the karst subsurface flow can only be achieved using an integrated soil–epikarst system perspective. Most previous studies focused exclusively on the soil layer or a soil–epikarst system that did not extend deep enough into the epikarst base. This limits a thorough understanding of the role that the soil–epikarst architecture system plays in the subsurface flow of landscapes underlain by carbonate rocks.

All of the studies identified were conducted in either sub-humid, semi-arid or Mediterranean karst areas (Leh et al., 2008; Wilcox et al., 2008; Li et al., 2011). These results are not able to represent humid subtropical karst near-surface hydrological regimes as karstification intensity is primarily controlled by the specific climatic hydrothermal conditions of the region (Klimchouk, 2004). Chandler and Bisogni (1999) conducted one of the few tropical humid karst area studies. Results indicated that forest clearance decreased both epikarst and soil surface water infiltration capacities leading to higher runoff. Subsurface flow is more prevalent in humid environment than drier climates as most studies have shown that subsurface flow occurs at saturated, or near saturated, conditions (Weiler et al., 2005). These considerations suggest that soil–epikarst architecture effects on subsurface flow generation remain poorly understood, and recent experimental data of subsurface flow for humid subtropical karst regions is very limited.

Karst terrain covers about 14% (1.3 million km^2) of China. Much (42%) is located in Southwest China, making this area the world's largest contiguous, humid, subtropical climate, karst area. Regional bedrock is primarily pure carbonate with an older stratum deposited during the Triassic period. It has a denser structure, lower porosity (<3%), and less hydrochloric acid (HCl) insoluble matter (<4%) than the sub-humid and semi-arid karst regions noted above (Yuan, 1994). Furthermore, high temperatures and abundant precipitation in humid subtropical areas results in their karst landscapes being classified as cockpit karst, which has been intensively affected by karstification dynamics and is characterized by similar dimension enclosed depressions surrounded by overlapping hills and ridges (Day, 2004; Chen et al., 2012; Huang et al., 2014).

Cockpit karst is the most typical landscape style present in Southwest China. Locally called “fengcong” (Chen et al., 2012; Huang et al., 2014) (Fig. 1), it is markedly different from either Edwards Plateau, or Mediterranean, karst as they have relatively gentle terrains. The flat depression area suitable for human habitation and cultivation in cockpit karst areas of Southwest China is less than 50% of the entirety. Most of the catchment area has a 20% or greater slope. High population densities create socioeconomic pressures. Excessive use of land for agriculture makes karst rocky desertification to be the most severe ecological issue threatening this region (Bai et al., 2013; Xu et al., 2015; Yan and Cai, 2015). Much of the footslope land (the base of the cone karst) adjacent to the depressions had heavily forested, but has been cleared for human utilization. The soils of this footslope land are shallow and usually underlain by highly irregular epikarst surface (Peng and Wang, 2012). These soil–epikarst architectural features resemble other non-karst landforms where shallow soil is underlain by undulate bedrock having a high subsurface flow generation potential (Weiler et al., 2005; Hopp and McDonnell, 2009).

Karst-region soil–bedrock architectures have unique characteristics due to karstification which do not exist at other geological areas (Klimchouk, 2004). Surficial karst processes facilitate the solutional enlargement of carbonate rock fissures, resulting in increased bedrock permeability. These processes also produce an irregular, pitted and etched epikarst sub-surface that increases epikarst surface topographical irregularity (Zhou and Beck, 2011). Recent studies suggest that subsurface topography and bedrock permeability were major factors influencing the threshold behavior of subsurface flow at the hillslope scale (Hopp and McDonnell, 2009; Graham et al., 2010). Whether subsurface topography and bedrock permeability also exert their effects on near-surface hydrological processes of karst hillslopes is unknown. If they do, then to what extent, and how, are questions remaining to be answered.

This study for the first time [to our knowledge] from an integrated soil–epikarst system perspective, conducted plot-scale, in situ, rainfall simulation experiments to investigate subsurface flow regimes in a humid sub-tropical cockpit karst region. A trench excavated to the epikarst lower boundary allowed the simultaneously identification of flow pathways in soil and epikarst zones. This method facilitated evaluation of subsurface flow regimes in an integrated soil–epikarst system which extended from the shrub-top to epikarst base. The primary objectives of this study were to: (1) understand of the nature and origin of subsurface flow processes occurring in a soil-mantled sub-tropical dolomite karst slope; and, (2) analyze how the integrated soil–epikarst architecture system, initial moisture conditions, and rainfall intensity, effect subsurface flow onset, rate, and spatio-temporal patterns.

2. Materials and methods

2.1. Study site

The experiments were conducted in the Mulian catchment located in Huanjiang County of northwest Guangxi, in Southwest China (Fig. 2a). It is an area of 1.14 km^2 used for long-term field research by the Huanjiang Observation and Research Station for Karst Ecosystems of the Chinese Academy of Science. It is a representative cockpit karst catchment developed on dolomite and characterized by a flat depression (28% of the total catchment area) surrounded by overlapping hills and ridges except for an outlet in its northeast (Fig. 2a, b). About 60% of slopes have a gradient greater than 25°. Elevation ranges from 272 to 647 m above sea level. The climate is classified as sub-tropical, with

Fig. 1. Typical landscape of cockpit karst (fengcong) in Southwest China.

monsoons and a mean annual rainfall of approximately 1389 mm mostly falling between May to September. The annual average air temperature is 18.5 °C with monthly average temperature increasing from 10.1 °C in January to 28.0 °C in July.

2.2. Trench site and experimental plot

Excavations at experimental hillslopes have been a common method for quantifying subsurface stormflow and water mixing in response to storm rainfall (Kirkby, 1978; Dasgupta et al., 2006; Tromp-van Meerveld and McDonnell, 2006). In order to study karst hillslope hydrology, an 80 m trench running perpendicular to the western footslope, having an average vertical depth of 4 m and located near the lower epikarst boundary (no visible rock fractures and conduits, with a steady infiltration rate less than 3 mm h^{-1}), was excavated by backhoe between February to May 2013 (Fig. 2b). The trench site epikarst was only moderately weathered under a shallow soil mantle with relatively low solubility, well-indurated dolomite bedrock (Fu et al., under review). Except for one solutionally-widened joint, there were few voids, or fractures, in the epikarst of the experimental area (Table 1). Therefore, plant roots were generally restricted to the soil layer, rarely penetrating the underlying epikarst system (Fig. 2c).

The experimental plot was located in the footslope of a slightly concave hillslope, thus the surface drainage area was only determined by the sprinkling area. Thus, there was no need to install metal sheets at the edges of the experimental plot to restrict the experimental area. A projected sprinkling circular area (R = 2.5 m) of about 19.6 m^2 was expected for our rainfall simulator; therefore the actual area of our experimental plot was 20.1 m^2 when taking into account the average slope of 23.5% (Fig. 2b). A 50 cm upslope buffering band between the lower boundary of the experimental plot and the trench face was maintained to ensure that simulated rainfall did not affect overland flow and subsurface flow collection on the lower slope. Vegetation consisted mainly of shrubs, herbs and vines which were the most common vegetation present in this karst environment (Fig. 2b). The total vegetation coverage was more than 90%, with shrubs being dominant. Vegetation height was less than 2.5 m and trunk diameter less than 4 cm. A litter layer about 1.5 cm thick overlaid about 95% of the soil surface. Soil was typically black calcareous soil of Inceptisol averaging 59 cm (CV = 48%) in depth and presenting a relatively smooth surface topography. By contrast, the underlying epikarst had a highly irregular surface topography and an abrupt contact with the overlying soil (Figs. 2b, 3). A narrow zone of epikarst outcrop occurred on the upslope, although most of the epikarst was soil covered.

The diameter of the circular experimental plot was 5 m. The actual length of trench face-generated flow was 7 m. To ensure that all of the runoff that flowed laterally out of the underground was collected during the simulated rainfall events, a 9 m-long trench face was equipped for flow collection and observation (Fig. 2c). A small concreted ditch, 5 cm below the soil–epikarst interface, was constructed following the undulate epikarst surface in order to collect subsurface flow. In order to get more data on the spatial variation of subsurface flow, this ditch was sub-divided into five sections according to each local epikarst surface topography. Then subsurface flow 1 (SSF1) to subsurface flow 5 (SSF5) were collected. In addition, another small concrete ditch was constructed at the bottom of the trench face to collect epikarst seepage flow. A soil pipe with a 4 cm diameter was located in the section for SSF4. It was monitored separately for pipe flow during the rainfall simulation experiments. A gutter was built on the right side of the experimental plot to route overland flow (Fig. 2c).

A total of 9 soil samples were collected from the upper, middle, and, lower parts of the experimental plots with three repetitions at each position. The pipette method was used to analyze soil texture. Total porosity (*TP*), capillary porosity (*CP*) and non-capillary porosity (*NCP*) were determined from undisturbed samples in 100 cm^3 cylinders using the water suction method (Liu et al., 1996), and the saturated hydraulic conductivity (*Ks*) with constant head method based on Darcy's law (Gwenzi et al., 2011). Disturbed soils were air-dried and then sieved through a 0.15 mm mesh to measure soil organic matter content using the potassium dichromate heating method (Bao, 2005). The rock fragment percentages (>2 mm) by soil mass were measured by separating the stones with a 2 mm sieve. Table 1 gives the main properties of soil and epikarst of the experimental plot.

2.3. Experimental treatments and rainfall simulations

Four rainfall simulation experiments were carried out to elucidate the effect of rainfall intensity and initial moisture conditions on the near-surface hydrological processes of the experimental plot. There were: high rainfall intensity with wet initial condition (HIGH-WET);

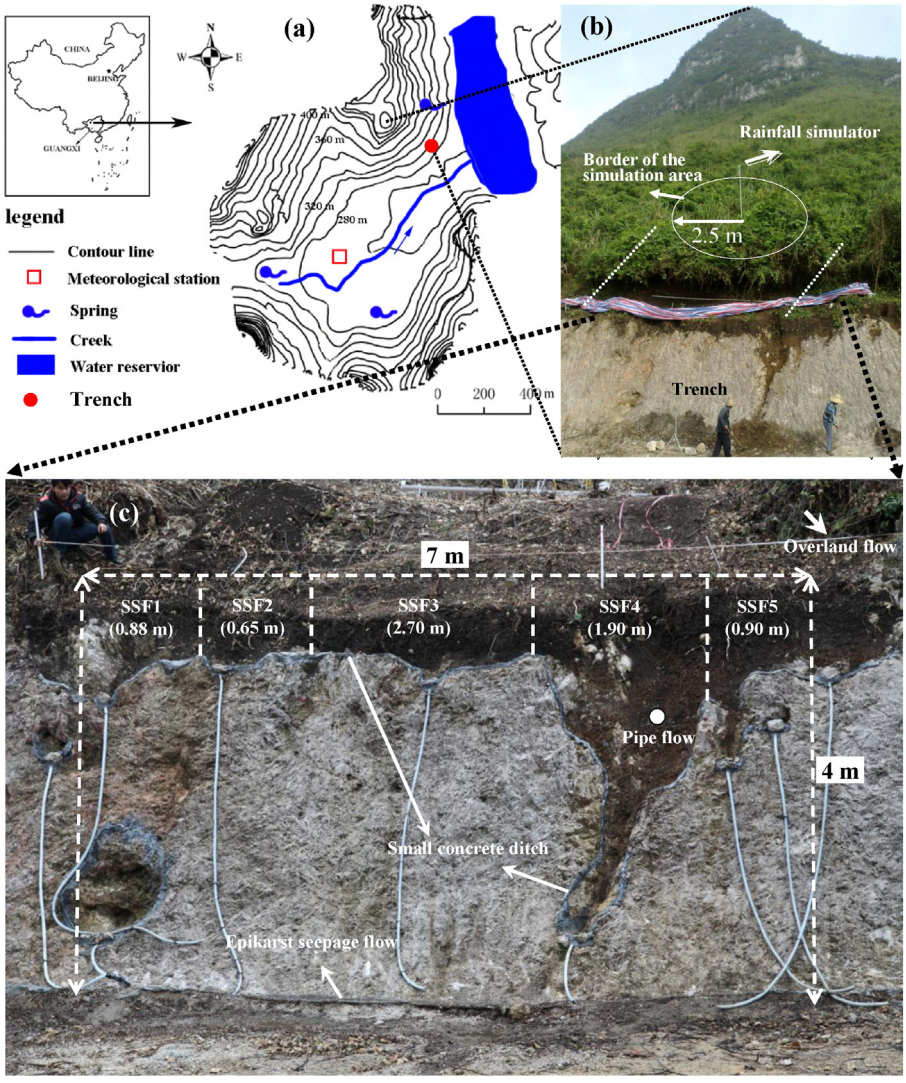

Fig. 2. (a) Topographical map of Huanjiang catchment; (b) photograph of the experimental hillslope showing experimental set-up. White dashed lines show the locations of the left and right upslope transects for measuring surface and epikarst surface topography excavated after the experiments; (c) trench face view showing: overland flow routing gutters; epikarst seepage flow; and sections for individual subsurface flow collection (SSF1 to SSF5) via small concrete ditches.

Table 1
Soil and epikarst properties of the experimental plot.

	Depth (cm)			
	0–10	10–20	20–30	30–50
Soil properties				
Rock fragment content (%)	7.4	12.8	4.1	2.3
Sand content (%)	28.1	27.2	28.1	29.2
Silt content (%)	43.7	39.3	35.8	36.6
Clay content (%)	28.3	33.5	36.2	34.3
Bulk density (g cm^{-3})	1.0	1.1	1.1	1.0
Total porosity (%)	62.3	58.1	59.6	61.1
Capillary porosity (%)	48.4	41.5	41.7	41.9
Non-capillary porosity (%)	9.5	8.1	9.6	8.1
Saturated hydraulic conductivity (mm h^{-1})	174.2	60.4	42.0	51.2
pH (1:2.5)	7.7	7.8	8.0	8.5
Soil organic matter content (%)	5.2	3.5	3.4	3.8
Epikarst rock properties				
Bulk density (g cm^{-3})	2.45	–	–	–
Total porosity (%)	7	8	4	3
Number of visible fractures per meter of trench length	3	2	0	0
Saturated hydraulic conductivity (mm h^{-1})	16	–	–	–

high rainfall intensity with dry initial condition (HIGH-DRY); low rainfall intensity with wet initial condition (LOW-WET); and low rainfall intensity with dry initial condition (LOW-DRY) (Table 2). The high (40 mm h^{-1}) and low (120 mm h^{-1}) rainfall intensities correspond to medium and high intensity rainstorms in the study area. The two different initial moisture conditions were obtained as follows. For the dry initial condition, the soil received no natural rainfall for at least 2 weeks prior to the sprinkling experiment. For the wet initial condition, the soil was sprinkled in an intensity of about 80 mm h^{-1} until any runoff commenced (around 250 mm of water) one day prior to the experiment (Table 2).

A portable rainfall simulator adapted from the design of Luk et al. (1986) was used to simulate rainfall with a manifold that feeds four SPRACO cone jet nozzles mounted 7 m above the soil surface (Fig. 2b). We carried out indoor parameter determination and accuracy testing for this rainfall simulator. The simulator applies water at rates ranging from 40 mm h^{-1} to 160 mm h^{-1}. When the operating pressure was set at 0.09 MPa, the median volume drop size was 2.4 mm with a uniformity of 80%. The water inlet pipe was connected with a water meter to measure the amount of water applied.

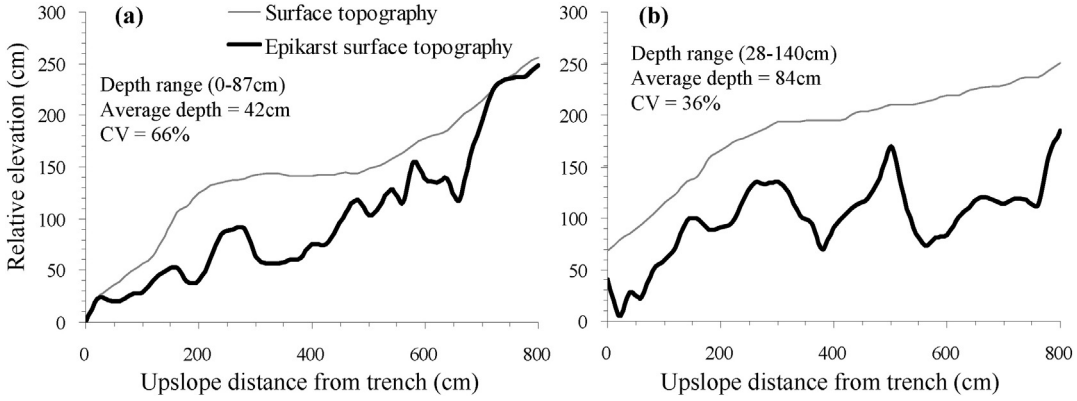

Fig. 3. Surface and epikarst surface topography on the left (a) and right (b) upslope transects across the rainfall simulation area. Transect locations are shown in Fig. 2(b) as white dashed lines.

Simulated rainfall was applied for each rainfall simulation experiment until a near steady runoff rate was reached. Due to the limited water supplies and unfavorable weather conditions, the field rainfall simulation experiments, ranging in duration from 2.4 h to 8.4 h (Table 3), were performed during the period of June to November 2013. The vegetation of the study area is mainly evergreen shrubs, providing very high coverage throughout the year. Although performed over a long period, the coverage conditions resulted in no significant differences between different rainfall simulation events (Table 2).

Each individual flow was routed into a plastic bucket through plastic pipes with their weight measured manually at 2-minute intervals in the beginning then gradually increasing to 20 min later. Accumulated rainfall amounts were also recorded manually from the water meter at the same frequency as that of water volume measurements.

Table 2
Experimental treatments and general experimental conditions before each rainfall simulation.

Variable	Experimental treatments			
	HIGH-WET	HIGH-DRY	LOW-WET	LOW-DRY
Date	31-5-2013	18-7-2013	20-7-2013	23-11-2013
Shrub cover (%)	92	97	97	90
Herbaceous cover (%)	15	25	25	15
Vine cover (%)	30	53	53	40
Litter coverage (%)	95	95	95	95
Dry weight of litter per unit area (kg m^{-2})	1.20	1.15	1.18	1.36
Outcrops cover (%)	8	8	8	8
Average slope (%)	23.5	23.5	23.5	23.5
Average soil volume estimated from transects (m^3)	16.28	16.28	16.28	16.28
Average epikarst depression volume estimated from transects (m^3)	4.09	4.09	4.09	4.09
Average soil depth (cm)	59	59	59	59
Average epikarst depression depth (cm)	15	15	15	15
Pre-wetting rain (mm)	245	0	261	0
Initial volumetric soil moisture (cm^3 cm^{-3})	0.320	0.232	0.309	0.245
Volumetric soil moisture after rainfall events (cm^3 cm^{-3})	0.384	0.349	0.387	0.379
Initial litter water content (%)	128.67	65.19	134.35	59.32
Litter water content after rainfall events (%)	210.00	191.00	197.00	202.00
Designed rainfall intensity (mm h^{-1})	120	120	40	40

HIGH: high rainfall intensity; LOW: low rainfall intensity; WET: wet initial condition; and DRY: dry initial condition.

2.4. Water balance calculation and data analysis

In this study, we presented a conceptual model of water balance for an integrated vegetation–soil–epikarst system. The fundamental water balance equations are:

$$P = I_c + I_l + S + OF + ET + SSF + E_f + E_h + E_s + D \quad (1)$$

$$\frac{d(P)}{d(t)} = \frac{d(I_c)}{d(t)} + \frac{d(I_l)}{d(t)} + \frac{d(S)}{d(t)} + \frac{d(OF)}{d(t)} + \frac{d(ET)}{d(t)} + \frac{d(SSF)}{d(t)} + \frac{d(E_f)}{d(t)} + \frac{d(E_h)}{d(t)} + \frac{d(E_s)}{d(t)} + \frac{d(D)}{d(t)} \quad (2)$$

Table 3
Rainfall, evapotranspiration, and hydrograph characteristics for each experimental treatment.

Variable	HIGH-WET	HIGH-DRY	LOW-WET	LOW-DRY
Rainfall characteristics				
Total rainfall (mm)	263.81	428.99	166.72	440.11
Average intensity (mm h^{-1})	110.07	118.61	40.66	52.30
Rainfall duration (h)	2.39	3.61	4.10	8.40
Pre-wetting rain (mm)	245.00	0.00	261.00	0.00
Average daily climatic variables				
Maximum air temperature (°C)	26.1	31.4	31.8	18.5
Minimum air temperature (°C)	20.0	23.8	23.1	13.5
Relative humidity (%)	95.33	86.33	85.33	97.67
Wind speed (m s^{-1})	0.26	0.33	0.48	2.30
Sunshine duration (h)	4.80	9.10	9.50	5.90
Potential evapotranspiration (mm day^{-1})	3.38	4.90	4.99	1.55
Estimated evapotranspiration during events (mm)	0.67	1.47	1.70	1.09
Total subsurface flow characteristics				
Time to outlet (h)	0.63	1.88	1.57	5.78
Threshold rainfall depth (mm)	69.71	223.39	63.70	302.47
Time to peak (h)	2.25	3.55	3.68	8.40
Accumulated rainfall to peak (mm)	248.19	421.11	149.78	439.57
Rate of peak flow (mm h^{-1})	56.27	68.48	14.74	21.32
Time of cessation (h)	12.67	10.50	14.43	13.97
Recession duration (h)	10.28	6.89	10.33	5.56
Runoff rate above threshold (mm runoff/mm rain)	0.29	0.32	0.23	0.25
Overland flow				
Threshold rainfall depth (mm)	67.73	254.03	–	–
Runoff rate above threshold (mm runoff/mm rain)	0.20	0.05	–	–
Total runoff rate above threshold (mm runoff/mm rain)	0.49	0.37	0.23	0.25

where P = simulated rainfall (mm); I_c = interception loss from canopy; I_l = litter interception (mm); S = soil storage (mm); OF = overland flow (mm); ET = evapotranspiration (mm); SSF = total subsurface flow (mm); E_f = depression filling on epikarst surface (mm); E_h = water held by epikarst (mm); E_s = epikarst seepage flow (mm); D = deep percolation (mm); and t = time since start of event (h).

Rainfall is the most important controlled variable during the simulated events, and wind interference must be avoided. Only the days of perfect weather conditions were selected for conducting simulation experiments. This is one of the reasons why the simulation experiments took so long (June until November 2013). By doing so, the actual daily average wind speed was less than 3 m s^{-1} during each rainfall simulation experiment (Table 3). Although each rainfall simulation experiment was performed in the early morning (usually started before 6:00 AM) with little wind interference, wind appearance was inevitable at some times due to the long simulation duration. However, it was observed that weak winds did not cause obvious loss of rainfall water by wind drift, mainly due to the high kinetic energy of raindrops in our rainfall simulation events with intensities greater than 40 mm h^{-1}. No significant loss of rainfall water was also confirmed from the similar hydrograph shape between two simulation events with identical rainfall intensity, which is illustrated in the following result section. Therefore, rainfall could be quantified by measurements of the supplied water from the water meter when neglecting the wind drift effect. The actual rainfall intensity of a certain period of time was then calculated as accumulated rainfall amount per unit of time divided by the sprinkling area of 19.6 m^2.

For understanding the hydrologic function of typical vegetation in karstic environment, since 2012 October, three shrub-dominated quadrats within the study catchment had been instrumented for measuring throughfall, interception loss and stemflow under natural rainfall events. A total of 28 rainfall events were measured between May and November 2013 (Fig. 4). Vegetation could obtain a maximal interception capacity during high rainfall amounts or duration events. Interception loss to the canopy in our simulation events was estimated as 5 mm based on these observed data (Fig. 4). Litter interception per unit area was estimated in situ by weighing three nylon net bags, each containing all litter from a 20 cm × 20 cm zone before and after each simulation (Table 2).

Three 15 cm-long TDR100 probes series were installed in the upper, middle, and lower slope positions to measure initial and final volumetric soil moisture in 0–15 cm, 15–30 cm and 30–45 cm soil layers by connecting a laptop to the TDR100. Disturbance to the experimental plot was minimized by driving each probe vertically into the bottom of a well hole which was pre-excavated down to the desired soil depths with a soil auger. Although experimental plot average soil depth was about 60 cm, driving the probe below 45 cm was unachievable because TDR probes ran into hard irregular epikarst surfaces at this depth.

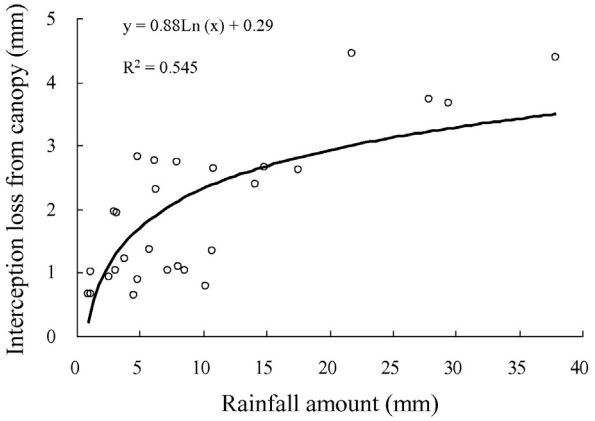

Fig. 4. Relationship between rainfall amount and interception loss from canopy.

Considering the homogeneous soil profile and a thorough wetting process, the 'per depth' water-holding volume of the 0–45 cm soil layer can represent the average soil holding capacity for the experimental plot. In addition, the measured soil water in the 0–45 cm soil layer was the capillary holding water and excluded the gravity water that usually perched on the soil–epikarst interface at a vertical depth below 45 cm. Thus, the measured soil water data reflected only the soil storage and excluded the epikarst-depression storage. The cross-sectional area of the soil and the maximum epikarst-depression was measured with AutoCAD according to the sectional drawings of transects 1 and 2 in Fig. 3. Their respective cross-sectional areas were then multiplied by the experimental plot width of 5 m to calculate their respective volume. The averaged increment of volumetric soil water content after each simulation event was multiplied by total soil volume of the experimental plot to calculate soil stored water (Table 2).

Potential evapotranspiration was calculated for the days when rainfall simulations were conducted using FAO-56 PM (Penman–Monteith) Method (Trajkovic and Kolakovic, 2009). Average 24-hour climatic data of wind speed, air temperature, relative humidity and sunshine duration, recorded at the catchment meteorological station, were used as inputs for the Penman–Monteith equation. Evapotranspiration during each rainfall simulation event was then estimated assuming an even distribution of the daily potential evapotranspiration through the daytime (Table 3).

All of the runoff components, including overland flow, individual subsurface flows (SSF1 to SSF5), and epikarst seepage flow, were measured manually as mentioned above. In this study, the relative contribution between epikarst depression-filling water held by epikarst and deep percolation was not distinguished. Their sum was thus defined as the "below epikarst surface components" including: 1) depression filling on epikarst surface (E_f); 2) water held by epikarst (E_h); 3) epikarst seepage flow (E_s); and 4) deep percolation (D), and was estimated by the water balance among different components.

$$E_f + E_h + E_s + D = P - S - I_c - I_l - OF - ET - SSF. \tag{3}$$

In order to estimate the steady infiltration rate at the soil–epikarst boundary, a new variable, which was defined as the difference between rainfall intensity and total runoff rate (the sum of the overland flow rate and subsurface flow rate), was introduced in the study:

$$\frac{d(P-OF-SSF)}{d(t)} = \frac{d(I_c)}{d(t)} + \frac{d(I_l)}{d(t)} + \frac{d(S)}{d(t)} + \frac{d(ET)}{d(t)} + \frac{d(E_f)}{d(t)} + \frac{d(E_h)}{d(t)} + \frac{d(E_s)}{d(t)} + \frac{d(D)}{d(t)}. \tag{4}$$

When a near-steady runoff rate is reached, it was assumed that:

$$\frac{d(S)}{d(t)} = 0;\ \frac{d(I_c)}{d(t)} = 0;\ \frac{d(I_l)}{d(t)} = 0;\ \frac{d(E_f)}{d(t)} = 0;\ \frac{d(ET)}{d(t)} = 0.$$

Then the steady infiltration rate at the soil–epikarst boundary can be estimated as:

$$\frac{d(P-OF-SSF)}{d(t)} = \frac{d(E_s + E_h + D)}{d(t)}. \tag{5}$$

The least significant difference (LSD) procedure (Student t-test) was used to compare the significant mean differences among the treatments for subsurface flow response variables and determined at $p < 0.05$ (Statistical Package for the Social Sciences Inc., 2001).

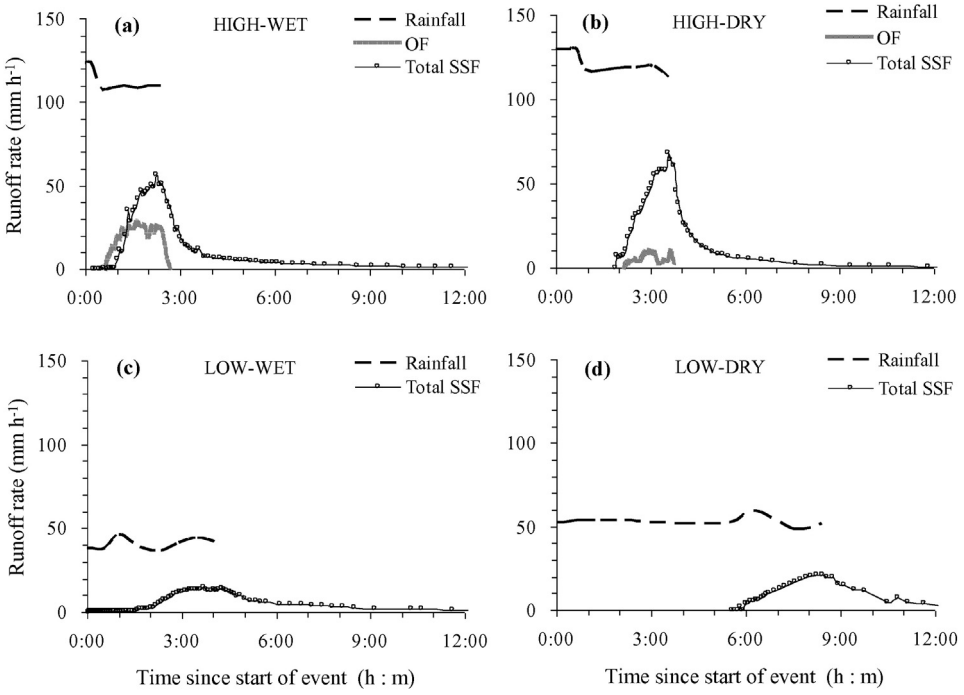

Fig. 5. Hydrographs of overland flow (OF) and total subsurface flow (SSF) for the four experimental treatments: (a) HIGH-WET; (b) HIGH-DRY; (c) LOW-WET; (d) and, LOW-DRY.

3. Results

3.1. Runoff hydrographs

Due to voltage instability, a variability of between 16% and 5% from the target intensity were observed for the rainfall simulations during low and high rainfall intensity events (Table 3). Fig. 5 illustrates runoff hydrographs for the four treatments consisting of overland flow and total subsurface flow. Subsurface flow dominated runoff processes in all rainfall events. Overland flow was observed only during high rainfall intensity events. Dry initial condition and low rainfall intensity both impeded overland flow generation. Overland flow and subsurface flow occurred almost simultaneously, suggesting that the experiment plot produced saturation-excess overland flow.

Subsurface flow began within 1 to 6 h after each rainfall simulation onset. It was more responsive to incoming rainfall under high rainfall intensity events than low rainfall intensity events (Fig. 5). Using the discharge stage separation method for subsurface flow proposed by Guebert and Gardner (2001), recession of subsurface flow occurred in three declining stages during high rainfall intensity events and two stages for low rainfall intensity events (Fig. 6).

The subsurface flow hydrograph shape was strongly influenced by rainfall intensity but it showed almost no difference between the wet and dry initial conditions for identical rainfall intensities (Fig. 6). Subsurface flow hydrographs flattened in lower rainfall intensity events compared to higher rainfall intensity events. Table 3 shows that peak flow rate declined from 56–68 mm h^{-1} to 15–21 mm h^{-1} when rainfall intensity decreased from 110–119 mm h^{-1} to 41–52 mm h^{-1}. If rainfall intensity was at the same level, subsurface flow hydrographs were almost the same between simulated events with different initial moisture conditions, excepting for a delayed onset of subsurface flow for the events with initial dry conditions (Fig. 6). This suggests that the dominant mechanism of the subsurface flow was saturated subsurface flow.

3.2. Subsurface flow coefficient and soil–epikarst interface permeability

Subsurface flow would not initiate if a threshold rainfall depth was not reached (Fig. 7). Threshold rainfall depth relied on the initial moisture conditions, showing little influence from rainfall intensity. It had an average value of 67 mm and 263 mm for wet and dry initial conditions, respectively. By contrast, steady-state subsurface flow coefficients were mainly influenced by rainfall intensity, showing little dependence upon initial moisture conditions. These coefficients had an average value of 0.52 and 0.36 for high and low rainfall intensity events, respectively (Fig. 7).

Based on Eqs. (4) and (5), Fig. 8 shows the trends of the difference between rainfall intensity and total runoff rate (the sum of the overland

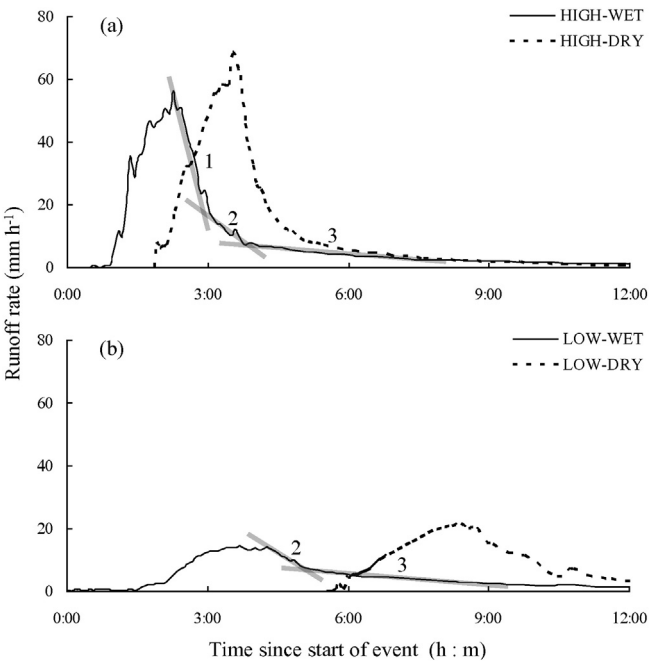

Fig. 6. Subsurface flow hydrographs under high (a) and low (b) rainfall intensities. Hydrographs exhibit flattening and translation effects responding to low rainfall intensity and dry initial condition, respectively. The gray bars indicate stages of subsurface flow discharge.

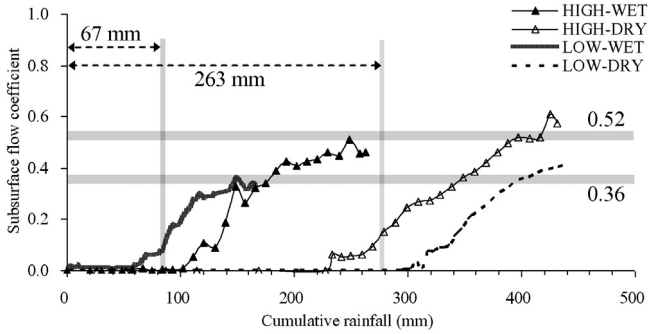

Fig. 7. Relationships between total subsurface flow coefficient and cumulative rainfall under different experimental treatments. The vertical gray lines are the average threshold cumulative rainfall values needed to activate subsurface flow under wet (left) and dry (right) initial conditions. The horizontal gray bands show average steady-state subsurface flow coefficients values under high (upper) and low (below) rainfall intensity conditions.

flow rate and subsurface flow rate) under different experimental treatments. Regardless of initial and boundary conditions, all simulated rainfall events achieved a near-steady infiltration rate of about 35 mm h^{-1} at the soil–epikarst boundary by the end of each event (Fig. 8). This was lower than the minimal saturated hydraulic conductivity (42 mm h^{-1}) of the soil layers (Table 1). The experiments showed that almost all subsurface flow occurred in the epikarst surface. Taken together these indicate that the near steady infiltration rate shown in Fig. 8 was the soil–epikarst interface permeability capacity.

Subsurface flow rate above threshold, which represents the average increasing slope of the total subsurface flow during the rainfall event, was nearly identical in the rainfall events having similar rainfall intensity regardless of initial moisture conditions (Table 3). Particularly, it was nearly 1.5 times greater in high rainfall intensity events (0.31) than in low rainfall intensity events (0.24) (Table 3).

3.3. Volume and percentage of subsurface flow

Nearly twice as much rainfall was needed to reach a near steady-state flow during dry initial condition than during wet initial condition. Six different hydrological components could be identified: 1) overland flow; 2) soil storage and interception loss; 3) depression filling on epikarst surface; 4) subsurface flow; 5) deep percolation; and 6) water held by epikarst. Epikarst seepage flow was not generated under all experimental treatments (Fig. 9). Subsurface flow and the "below epikarst surface components" (calculated by Eq. (3) and indicated as (6) + (7) + (8) + (9) in Fig. 9) showed a reciprocal relationship. Both depended mainly on initial moisture conditions. In wet initial condition, 40% or more of the water applied exited the plots as subsurface flow. Overland flow was less than 15%. In dry initial condition, subsurface flow was less than 30% of water applied and overland flow was less than 2%.

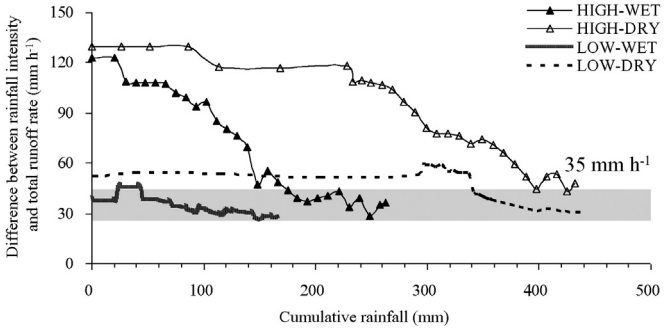

Fig. 8. Trends of difference between rainfall intensity and total runoff rate (the sum of the overland flow rate and subsurface flow rate) under different experimental treatments. The gray band illustrates that a similar steady infiltration rate of about 35 mm h^{-1} was reached at the soil–epikarst boundary, regardless of the experimental conditions.

3.4. Characteristics of individual subsurface flows

Fig. 10 provides hydrographs for individual subsurface flows and pipe flows for the four experimental treatments. Individual subsurface flows produced different hydrographs among each other even under identical experimental conditions (Fig. 10). Nevertheless, hydrographs for the same individual subsurface flow exhibited a flattening effect when rainfall intensity decreased and translation effect when initial moisture declined. All these characteristics were similar to those of the total subsurface flow described above.

The individual subsurface flow variables showed strong variability with coefficients of variation ranging from 12% to 102%, except for the time to peak flow and accumulated rainfall to peak flow which had coefficients of variation of less than 11%. The variables of time to peak flow and accumulated rainfall to peak flow reflected the rainfall depth needed to achieve hydrological connection between transient saturated areas of the whole experimental plot. This depended primarily on the overall plot architecture. Therefore, less variation was observed for these two variables. However, other variables were determined by specific characteristics of the location which displayed high soil–epikarst architecture heterogeneity among the different sections for collecting individual subsurface flows (Fig. 2c).

Per width percentage of contribution to total subsurface flow varied greatly (coefficient of variation >20%) among individual subsurface flows even under the same experimental conditions (Fig. 11). However, subsurface flow became more uniform across the trench as rainfall intensity increased and initial moisture condition became wetter. Much higher variability was observed between dry initial conditions (ranging from 69.8% to 104.7%) than wet initial conditions (ranging from 58.4% to 67.7%).

3.5. Impacts of initial moisture conditions and rainfall intensity on subsurface flow

Table 4 demonstrates the hydrologic response of individual subsurface flows to initial moisture conditions and rainfall intensity. Dry initial condition significantly increased the time to outlet, threshold rainfall depth, time to peak, and accumulated rainfall to peak, but decreased recession duration compared to those of wet initial condition. Rainfall intensity had a significant positive influence on the hydrologic parameters mainly related to flow rate. Specifically, high rainfall intensity significantly decreased time to outlet and time to peak, but increased peak flow rate and accumulated rainfall from outlet to peak when compared to low rainfall intensity.

Threshold rainfall depth and accumulated rainfall to peak represented the rainfall amounts required to generate runoff and to reach peak flow, respectively. Both were primarily determined by initial moisture conditions and affected little by rainfall intensity. Both were significantly reduced under the wet initial condition compared to the dry initial condition. However, accumulated rainfall from outlet to peak – which showed a decreasing trend as rainfall intensity decreased (Table 4) – exhibited a stronger dependence on rainfall intensity than on initial moisture conditions.

4. Discussion

4.1. Relevance of subsurface flow in cockpit karst hillslope

There is a general consensus that subsurface flow is the main runoff-generation mechanism in humid regions having steep terrains and conductive soils (Weiler et al., 2005). The experimental plot – a soil-mantled subtropical dolomite karst slope – was characterized by high steady-state subsurface flow coefficients with the rainfall amount as

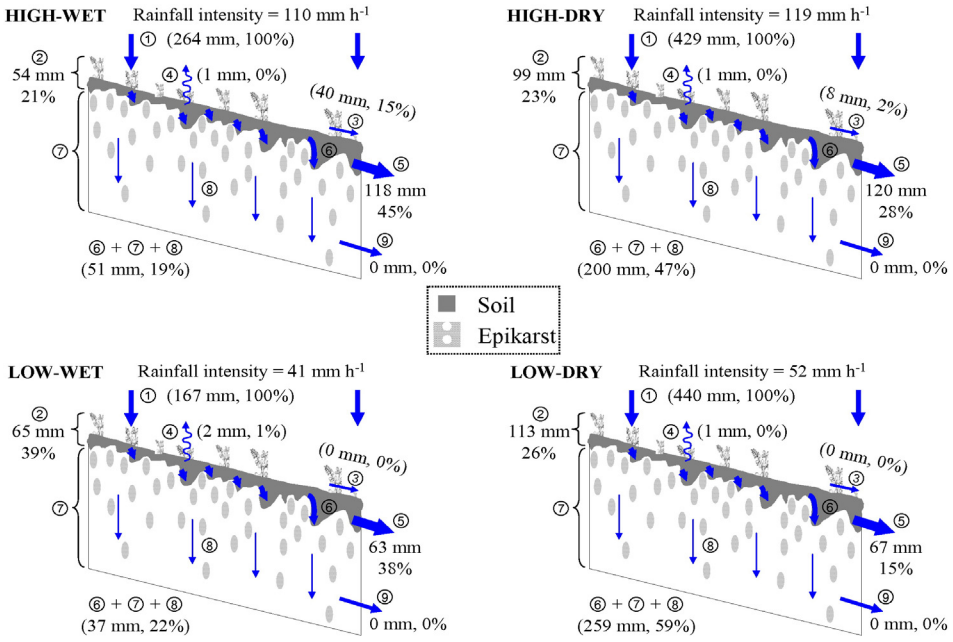

Fig. 9. Conceptual framework of hillslope flow pathways and rainfall partitioning under different experimental treatments: ① rainfall; ② soil storage and interception loss; ③ overland flow; ④ evapotranspiration; ⑤ subsurface flow; ⑥ depression filling on epikarst surface; ⑦ water held by epikarst; ⑧ deep percolation; and ⑨ epikarst seepage flow.

the main driver for runoff generation. These experiments are the first [to our knowledge] to demonstrate that subsurface flow may also be a dominant runoff-generation mechanism for a humid sub-tropical karst hillslope. Table 5 shows average values of extreme precipitation indices for the main provinces of Southwest China (Liu et al., 2014). In Guangxi, the region of the studied catchment, the expected maximum daily rainfalls with recurrence intervals of 10 years, 30 years and 100 years, are 180 mm, 228 mm and 295 mm, respectively. Accordingly, a daily 67 mm rainstorm (Fig. 7), which is required for runoff onset (both surface and subsurface) under initial wet conditions, has a recurrence interval of less than 10 years. This short recurrence interval indicates the importance of subsurface flow in cockpit karst under natural conditions. If we consider the 199 mm accumulated rainfall required for reaching the peak discharge of subsurface flow under initial wet condition (Table 3), a recurrence interval of about 10 years suggests subsurface flow may contribute to the extreme flood events in karst catchments. This, in turn, could exacerbate the increased flood risk in this area (Liu et al., 2014). The required threshold was 263 mm for onset of subsurface flow under initial dry condition (Fig. 7). This value approximates the maximum daily rainfall with a recurrence interval of 100 years (Table 5). Although the daily rainfall of this magnitude is rare under natural conditions, an annual maximum consecutive 5-day precipitation of 318 mm has a much shorter return period of only 10 years (Table 5). Considering that rainfall amount is the main driver for initiating saturation-excess runoff in our experimental plot, subsurface flow can be initiated during high consecutive precipitation events even under the initial dry condition.

Because footslopes are known to exert a vital influence on hydrologic connectivity between hillslopes and depression zone, the study here focused only on the near-surface hydrological processes of the footslope position based on plot-scale rainfall simulation experiments. If the experimental plot were to be extended to include the whole karst hillslope allowing the upslope runoff to run into the footslope, just as it does under natural rainfall events, the hillslope-scale required threshold rainfall depth for the onset of runoff may be much lower than the plot-scale threshold derived from our rainfall simulation experiments. In this sense, subsurface flow may occur even under the initial dry condition because high plot-scale threshold rainfall depth (Fig. 7) is reached relatively easily through both direct rainfall and indirect upslope runoff.

4.2. Fill and spill processes in subsurface flow generation

Extreme hillslope heterogeneity leads to highly complex dynamics of hillslope subsurface flow response (Weiler et al., 2005; Wilcox et al., 2007). There are many possible variables influencing subsurface flow. Field-based studies of subsurface flow, especially on steep slopes with thin soils overlaying irregular bedrock surface, showed that subsurface topography and bedrock permeability were two of the most important variables (Freer et al., 2002; Tromp-van Meerveld et al., 2007). Recent studies further suggested that sub-surface topography and bedrock permeability were also the main factors influencing threshold behavior of subsurface flow at the hillslope scale (Hopp and McDonnell, 2009; Graham et al., 2010).

In soil–bedrock architecture terms, most karst slopes are also characterized by a thin soil layer overlaying a highly irregular epikarst surface, which is similar with other landforms where shallow soil is underlain by undulating bedrock. However, the unique soil–bedrock architectural characteristics of karst regions result from karstification which does not exist at other geological sites (Klimchouk, 2004). First, karst hillslopes are characterized by thin soil patches discretely distributed along the hillslope resulting from the weak pedogenetic capacity of carbonate stone. In addition, the calcium-rich environment promotes a highly stable soil aggregate formation resulting in a high soil infiltration capacity. Second, epikarst surface topography is significantly more irregular than non-carbonate bedrock topography and can be attributed to the essentially different weathering processes of carbonate compared to non-carbonate bedrocks. Carbonate weathering processes are dominated by a heterogeneous chemical dissolution. Non-carbonate bedrock weathering processes are dominated by physical weathering. Soil is the main source for CO_2 production in karst hillslopes, thus carbonate rock surfaces directly contact the overlying soil and suffer the most intense chemical energies of karstification. These surficial karst processes enhance solutional enlargement of carbonate rocks fissures which, in turn, increases bedrock permeability while, simultaneously, producing an irregular, pitted and etched, epikarst sub-surface which intensifies

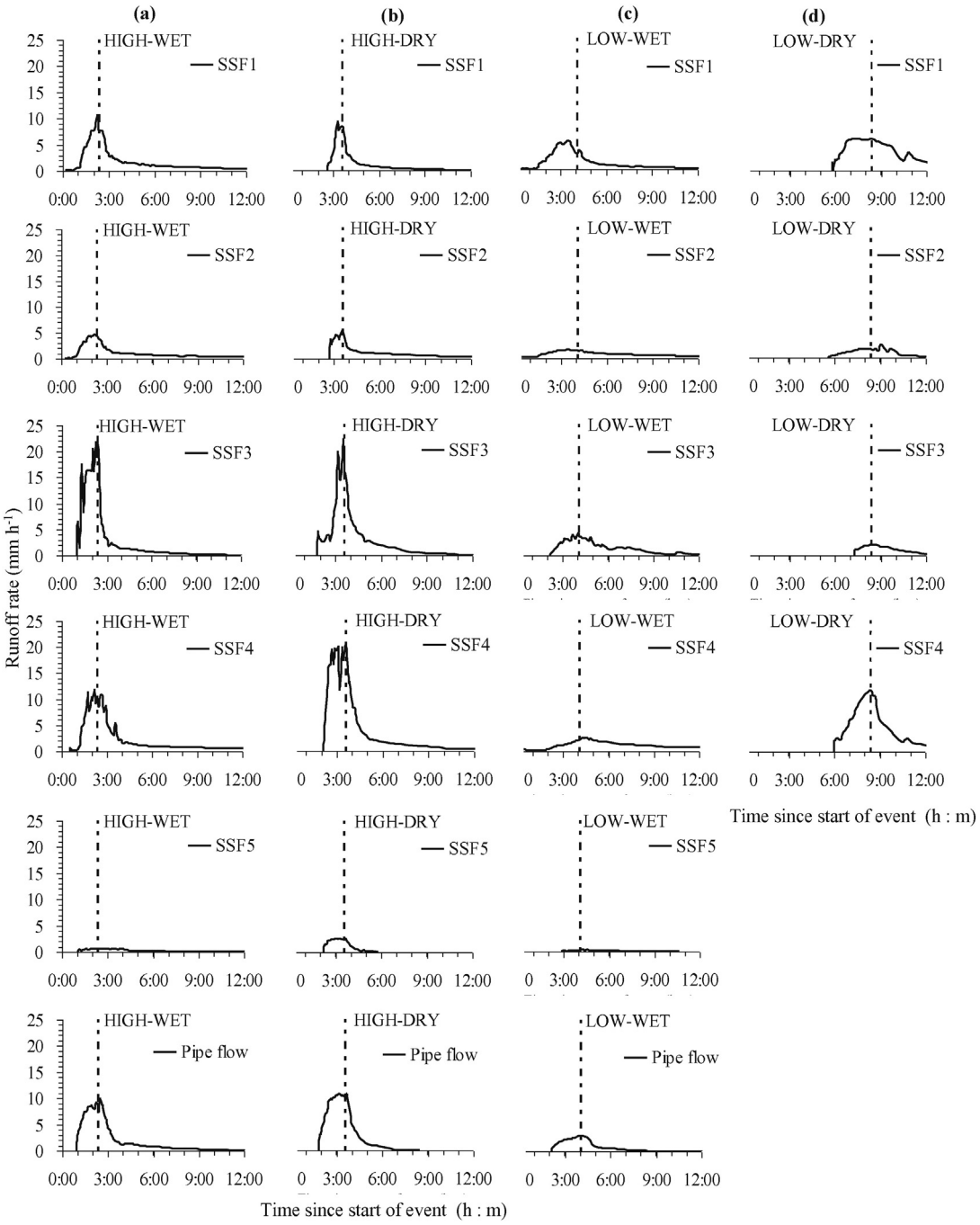

Fig. 10. Hydrographs of individual subsurface flows (SSF1 to SSF5) and pipe flow for the four experimental treatments: HIGH-WET (a), HIGH-DRY (b), LOW-WET (c), and LOW-DRY (d). The dashed vertical lines indicate simulated rainfalls cessation.

the irregularity of the epikarst surface topography (Zhou and Beck, 2011).

Although the underlying epikarst surface had a plot-scale relatively high infiltration capacity of about 35 mm h^{-1} (Fig. 8), the conductivity contrast between the soil and the epikarst surface at our experimental plot was sufficient for water to pond at the soil–epikarst interface during simulated rainfall. The epikarst surface acted as a sub-surface infiltration barrier resulting in perched water tables at epikarst surface depressions. Consequently, during large rainfall events, subsurface flow occurred laterally over the epikarst surface and vertically through the epikarst system. Water-filled depressions eventually connected with each other during the ongoing infiltrating rainfall. Fig. 12 shows the linear relationship between subsurface flow volume with maximum relative vertical depth of epikarst surface for each individual subsurface flow at the trench face. A positive linear ($r^2 = 0.54$) relationship (significant at $\alpha = 0.01$) can be seen between subsurface flow volume and maximum relative vertical depth of epikarst surface, indicating that the epikarst surface located at relatively lower levels was more inclined to concentrate subsurface flow. There were similar results in field-based hydrological investigations conducted in non-karst regions (Freer et al., 2002; Tromp-van Meerveld and McDonnell, 2006). Although the "maximum relative vertical depth of epikarst surface" proposed here differed from Freer's bedrock accumulated area (Freer et al., 2002), our result also confirmed, to an extent, that bedrock topography was the best surrogate for predicting subsurface flow volume since most of saturated subsurface flow was generated on the soil–bedrock surface (Freer et al., 2002; Tromp-van Meerveld and McDonnell, 2006).

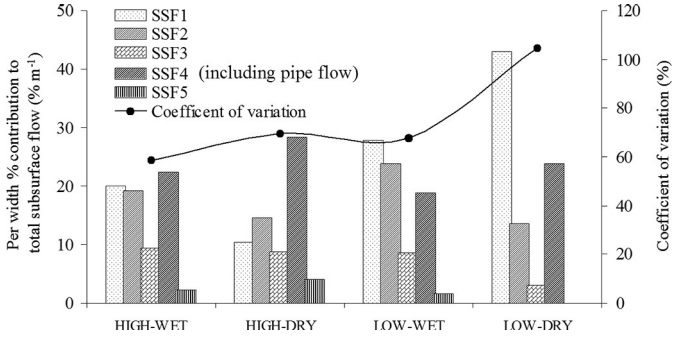

Fig. 11. Per width % contribution to total subsurface flow and variation coefficients of individual subsurface flow (SSF1 to SSF5) under different experimental treatments.

Table 5
Average values of extreme precipitation indices for the main provinces in Southwest China (after Liu et al., 2014).

Province	Num. of meteorological stations	R × 5 (10) (mm)[a]	CWD_{10} (day)[b]	Maximum daily rainfall (mm)		
				10 year return period	30 year return period	100 year return period
Guangxi	**23**	**318**	**12**	**180**	**228**	**295**
Guizhou	18	192	10	124	154	190
Yunnan	31	172	14	95	115	138

The numbers in bold indicate the average values of extreme precipitation indices for the region of the studied catchment.
[a] Annual maximum consecutive 5 day precipitation with return period of 10 years.
[b] Maximum number of consecutive days with precipitation with return period of 10 years.

Transects 1 and 2 were excavated directly upslope from subsurface flow collection sections for SSF1 and SSF4, respectively (Fig. 2). SSF1 and SSF4 hydrographs can thus be related to their corresponding soil–epikarst architecture using transect 1 and 2, making a tentative study of the 'fill and spill' hypothesis possible. It can be seen from Fig. 13 that both upslope transects have a similar soil–epikarst architecture consisting of four epikarst depression locations although transect 2 depression areas are larger than transect 1. It is well known soil or soil–epikarst architecture was the first order control of near-surface hydrological response in various temporal and spatial scales (Wilcox et al., 2007; Leh et al., 2008). This explains why the two upslope transects produced similar hydrograph shapes under the same initial and boundary condition (Fig. 13). How these similar subsurface flow hydrographs were produced by the fill and spill processes can be explained as follows. First, trench face observations suggest that most subsurface flow was generated at the soil–epikarst interface during simulated events, indicating that the subsurface flow process was saturation from below; a wetting up from the epikarst surface into the soil profile. It may be that epikarst surface topography rather than soil surface topography that controls subsurface flow generation for karst hillslopes like the study site. Since water perches at the soil–epikarst interface, this surface may determine the ultimate flow pathway and subsurface flow spatial pattern of an artificial trench. Second, extremely high threshold rainfall depth (up to 312 mm under initial dry condition) and greatly delayed subsurface flow suggest that epikarst depression-filling processes exist. These filling processes were further proved by the fact that higher epikarst depression depth led to higher depth of accumulated rainfall to peak, especially under the initial dry conditions (Fig. 13). The rapid increase in the flow rate indicates that spilling processes were triggered immediately after most epikarst depressions filled. The sharp decrease in the flow rate suggests that spilling processes ceased when rainfall ceased. These spilling processes were further demonstrated by the fact that a greater epikarst depression depth led to a greater subsurface flow peak as can be seen from Fig. 13.

This is speculation based on an assumption that subsurface flow is mainly determined by the soil–epikarst architectural characteristics of upslope trenches perpendicular to the contour line. Recent studies have found that the subsurface flow contribution area is mainly determined by bedrock topography rather than surface topography (Lanni et al., 2013). The fine details of epikarst surface contributing area may more adequately explain the subsurface flow spatial patterns of karst regions where sub-surface runoff dominates. The fill and spill hypothesis needs to be further examined in the karst regions through more detailed experimental study combining tracer, hydrometric and geophysical techniques.

4.3. Flow regimes of subsurface flow

Main subsurface flow regimes at the hillslope scale can be divided into matrix flow and preferential flow. In this experimental plot,

Table 4
Hydrologic response of individual subsurface flow to initial moisture conditions and rainfall intensity.[a]

Mean ± standard deviation for each experimental condition	Initial moisture conditions		Rainfall intensity		Average CV (%)
	WET	DRY	HIGH	LOW	
Volume (mm)	15.08a ± 9.34 (12, 61.89)[a]	18.75a ± 13.05 (10, 69.58)	19.84a ± 11.82 (12, 59.57)	13.04a ± 9.27 (10, 71.14)	65.55
Percentage relative to total rainfall depth (%)	6.88a ± 3.58 (12, 52.13)	4.33a ± 3.02 (10, 69.80)	6.06a ± 3.75 (12, 61.94)	5.31a ± 3.35 (10, 63.04)	61.73
Time to outlet (h)	**0.97B ± 0.95** (12, 98.34)	**3.82A ± 2.08** (10, 54.50)	**1.47b ± 0.90** (12, 61.25)	**3.22a ± 2.74** (10, 85.13)	74.80
Threshold rainfall depth (mm)	**63.04B ± 46.33** (12, 73.50)	**289.30A ± 49.58** (10, 17.14)	171.22a ± 108.71 (12, 63.49)	159.49a ± 146.90 (10, 92.11)	61.56
Time to peak (h)	**3.16B ± 0.91** (12, 28.80)	**5.44A ± 2.52** (10, 46.45)	**2.92B ± 0.63** (12, 21.69)	**5.73A ± 2.29** (10, 40.06)	34.25
Accumulated rainfall to peak (mm)	**206.36B ± 51.40** (12, 24.91)	**418.76A ± 23.00** (10, 5.49)	334.00a ± 84.61 (12, 25.33)	265.60a ± 139.70 (10, 52.60)	27.08
Rate of peak flow (mm h^{-1})	6.49a ± 6.42 (12, 98.91)	9.32a ± 7.23 (10, 77.49)	**10.98a ± 7.42** (12, 67.59)	**3.95b ± 3.21** (10, 81.28)	81.32
Recession duration (h)	**18.37a ± 5.84** (12, 31.78)	**10.70b ± 8.34** (10, 77.89)	16.65a ± 8.28 (12, 49.71)	12.77a ± 7.34 (10, 57.52)	54.23
Accumulated rainfall from outlet to peak (mm)	143.32a ± 53.48 (12, 37.31)	129.46a ± 47.12 (10, 36.40)	**162.77A ± 42.16** (12, 25.90)	**106.12B ± 41.41** (10, 39.02)	34.66
Average CV (%)	56.40a	50.53a	48.50a	64.65a	

LSD tests showing values within a row of different initial moisture conditions, or rainfall intensities followed by the different letter are significantly different. Upper case letter indicates significance at the 0.01 probability level, lower case letter at the 0.05 probability level.
The numbers printed in bold letters indicate a significant difference between experimental treatments.
[a] Sample number, coefficient of variation.

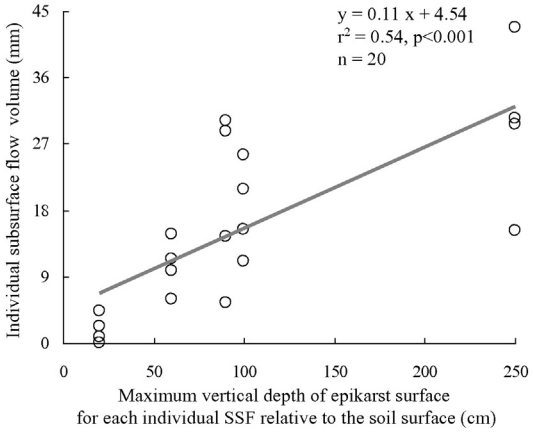

Fig. 12. Relationship of subsurface flow volume with maximum relative vertical depth of epikarst surface for each individual subsurface flow at the trench face.

subsurface flow was dominated by preferential flow. Soils developed in this experimental karst hillslope exhibited the architecture of a shallow soil layer abruptly in contact with the underlying epikarst surface. This is one of the main features of karst regions (Wilcox et al., 2007, 2008; Heilman et al., 2014). These soils usually show high aggregate stability and high organic content due to a calcium-rich environment (Dasgupta et al., 2006; Wilcox et al., 2008). These features combine with a dense root mass below the soil layer to create various preferential paths creating a high soil infiltration capacity which is greater than most normal rainfall intensities. The result is that infiltration-excess overland flow is rare in the study area (Chen et al., 2012; Peng and Wang, 2012). Subsurface flow occurred as lateral flow at the soil–epikarst interface with a fast hydrological response when threshold rainfall depth had reached. It quickly recessed after sprinkling had stopped (Fig. 5). These characteristics clearly proved that the subsurface flow in our experimental plot was dominated by preferential flow components.

In sub-humid, sub-tropical karst regions, Dasgupta et al. (2006) suggested that subsurface flow was also dominated by fast preferential flow. However, soil–epikarst architectural differences between the two study sites led to different preferential flow pathways. At Dasgupta's limestone experimental site, the epikarst was more developed and the soil–epikarst profile consisted of parallel geologic layers with rocky soils imbedded in various karstic features. Their work demonstrated that preferential flow resulted from both juniper root channels and planar fractures in the limestone. At our dolomite experimental plot, the biologically-rich and well-structured soil abruptly contacts the underlying consolidated epikarst, making a clear boundary between soil and epikarst (Fig. 2). Soil pipes, root channels and inter-aggregate pores together constructed a preferential network within the soil, thus preferential flow mainly originated from root channels and soil pipes but not from karst fractures. The distinctly different preferential flow pathways between these two karst systems not only indicate the hydrological heterogeneity and complexity of karst regions, but also the role

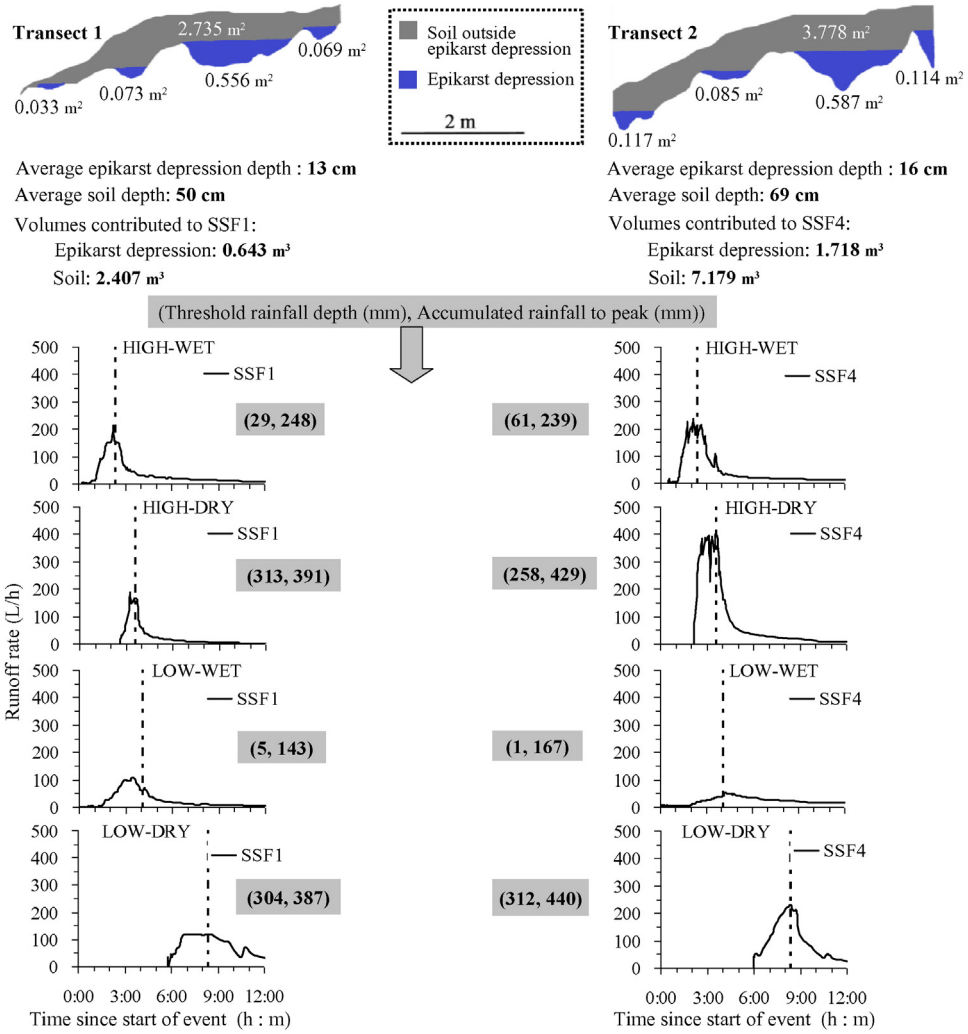

Fig. 13. Relation between SSF1 and SSF4 and their corresponding soil–epikarst architecture.

played by soil–epikarst architecture in determining near-surface hydrological processes of such regions.

4.4. Effect of permeable and highly irregular epikarst surface on subsurface flow

The more irregular sub-surface topography and higher bedrock permeability capacity enhance the threshold response phenomenon which can be explained by the filling and spilling mechanism proposed by Tromp-van Meerveld and McDonnell (2006). The irregular subsurface topography performs its role through the following process: 1) during rainfall events, transient saturation fills local depressions in the bedrock microtopography; 2) water then spills laterally over the bedrock ridges between depressions flowing further downslope through bedrock lows; and 3) depressions in the bedrock are filled and the saturated areas connect to each other resulting in significant subsurface flow. The permeable bedrock exerts its effects on these two aspects of 'filling and spilling'. On one hand, transient saturation at the soil–bedrock interface is delayed due to infiltration into the bedrock during rainfall events. On the other hand, bedrock leakage empties the bedrock depressions between rainfall events such that it has to be refilled again during the following rainfall event. Therefore, bedrock infiltration between rainstorms results in more storage being available by the next rainstorm and results in higher thresholds for subsurface flow and less subsurface flow (Tromp-van Meerveld et al., 2007).

In our experimental plot, the unique karstification process had greatly increased threshold rainfall depth through delaying the filling and spilling process from two routes. Horizontally, highly irregular epikarst surfaces created by differential dissolution of dolomite greatly increased depression-filling capacities. Vertically, cavities and integrated conduits produced by chemical dissolution greatly increased epikarst vertical drainage capacity. This explains why the threshold rainfall depth of the experimental plot (up to 302 mm) is much greater than for non-karst hillslopes (ranging from 20 mm to 60 mm) (Tani, 1997; Weiler et al., 2005).

The main soil–epikarst architectural characteristics change in a regular way during karst development (Klimchouk, 2004). This leads to distinct and unique hydrogeological behavior among different karst systems. Our experiment was conducted on a soil-mantled dolomite slope of relatively low karstification and thus was not representative of flow regimes for other karst regions having different geological features and climatic characteristics. For example, we suggest that if our study were to be conducted in a limestone area, or dolomite area, which had experienced more efficient and deeper karstification, then deep percolation would become a key hydrological process while the subsurface flow occurring at the soil–epikarst interface would decrease. Even so, the results of this study lend support to the idea that subsurface flow: 1) is an important runoff-generation mechanism in sub-tropical cockpit karst landscapes; and 2) is highly variable and dependent on epikarst surface permeability and topography, initial moisture conditions and rainfall intensity.

5. Conclusions

Using plot-scale field rainfall simulation experiments, our study investigated the subsurface flow processes in a humid, sub-tropical, cockpit karst region of Southwest China. A trench excavated to the epikarst lower boundary facilitated identification of subsurface flow regimes in an integrated soil–epikarst architecture system. We found that this dolomite karst shrubland hillslope was characterized by high steady-state subsurface flow coefficients (0.52 and 0.36 for high (114 mm h^{-1}) and low (46 mm h^{-1}) rainfall intensity events). Subsurface flow showed a strong variability and was dominated by preferential flow. Irregular epikarst surface and high epikarst vertical drainage capacity joined to result in a high threshold rainfall depth for subsurface flow (67 mm and 263 mm for wet and dry initial conditions). We propose the fill and spill hypothesis as a potential explanation for this threshold behavior in subsurface flow in cockpit karst hillslope.

Because these findings are based on only four rainfall simulation experiments on the foot slope of a dolomite karst hillslope, a strict generalization cannot be made that subsurface flow characterizes all different karst hillslopes or different hillslope positions. These findings, however, do lend strong support to the idea that subsurface flow: (1) is an important runoff generation mechanism in sub-tropical cockpit karst landscapes; and, (2) is highly variable, depending upon epikarst surface permeability and topography, initial moisture conditions and rainfall intensity. Further research should be focused on the identification of the spatial distribution characteristics of soil–epikarst architecture and associated hydrological functions along this cockpit karst hillslope.

Acknowledgments

This study was supported by the National Key Basic Research Program of China (2015CB452703), the National Natural Science Foundation of China (41301300 and 51379205), the Natural Science Foundation of Hunan Province, China (14JJ3144), and the CAS "Light of West China" Program (2012). The authors thank Prof. Artemi Cerdà and another anonymous reviewer for their valuable and constructive comments. Special thanks are also expressed to Weiwu Tang, Lijie Qin, Cong Huang, Ting Sun, and Xiaoyu Pan from Hechi University for their assistance in the fieldwork, and Stephen Laudig for checking the English of this paper.

References

Bai, X.Y., Wang, S.J., Xiong, K.N., 2013. Assessing spatial–temporal evolution processes of karst rocky desertification land: indications for restoration strategies. Land Degrad. Dev. 24, 47–56.
Bao, S.D., 2005. Soil Agriculturalization Analysis. 3rd ed. China Agriculture Press, Beijing, China.
Calvo-Cases, A., Boix-Fayos, C., Imeson, A.C., 2003. Runoff generation, sediment movement and soil water behaviour on calcareous (limestone) slopes of some Mediterranean environments in southeast Spain. Geomorphology 50, 269–291.
Cerdà, A., 1997a. Seasonal changes of the infiltration rates in a typical Mediterranean scrubland on limestone in southeast Spain. J. Hydrol. 198, 198–209.
Cerdà, A., 1997b. Soil erosion after land abandonment in a semiarid environment of southeastern Spain. Arid Land Res. Manag. 11, 163–176.
Cerdà, A., 1997c. The effect of patchy distribution of *Stipa tenacissima* L. on runoff and erosion. J. Arid Environ. 36, 37–51.
Cerdà, A., 1998a. Effect of climate on surface flow along a climatological gradient in Israel: a field rainfall simulation approach. J. Arid Environ. 38, 145–159.
Cerdà, A., 1998b. Relationship between climate and soil hydrological and erosional characteristics along climatic gradients in Mediterranean limestone areas. Geomorphology 25, 123–134.
Cerdà, A., 1998c. The influence of aspect and vegetation on seasonal changes in erosion under rainfall simulation on a clay soil in Spain. Can. J. Soil Sci. 78, 321–330.
Cerdà, A., 1998d. The influence of geomorphological position and vegetation cover on the erosional and hydrological processes on a Mediterranean hillslope. Hydrol. Process. 12, 661–671.
Cerdà, A., 1999. Parent material and vegetation affect soil erosion in eastern Spain. Soil Sci. Soc. Am. J. 63, 362–368.
Cerdà, A., 2001. Effects of rock fragment cover on soil infiltration, interrill runoff and erosion. Eur. J. Soil Sci. 52, 1–10.
Chandler, D.G., Bisogni Jr., J.J., 1999. The use of alkalinity as a conservative tracer in a study of near-surface hydrologic change in tropical karst. J. Hydrol. 216, 172–182.
Chen, H.S., Liu, J.W., Zhang, W., Wang, K.L., 2012. Soil hydraulic properties on the steep karst hillslopes in northwest Guangxi, China. Environ. Earth Sci. 66, 371–379.
Dasgupta, S., Mohanty, B.P., Kohne, J.M., 2006. Impacts of juniper vegetation and karst geology on subsurface flow processes in the Edwards Plateau, Texas. Vadose Zone J. 5, 1076–1085.
Day, M.J., 2004. Cone karst. In: Gunn, J. (Ed.), Encyclopedia of Caves and Karst Science. Fitzroy Dearborn, New York, pp. 241–243.
Estrada-Medina, H., Graham, R.C., Allen, M.F., Jimenez-Osornio, J.J., Robles-Casolco, S., 2013. The importance of limestone bedrock and dissolution karst features on tree root distribution in northern Yucatan, Mexico. Plant Soil 362, 37–50.
Feng, T., Chen, H.S., Wang, K.L., Zhang, W., Qi, X.K., 2014. Modelling soil erosion using a spatially distributed model in a karst catchment of northwest Guangxi, China. Earth Surf. Process. Landf. 39, 2121–2130.
Freer, J., McDonnell, J.J., Beven, K.J., Peters, N.E., Burns, D.A., Hooper, R.P., Aulenbach, B., 2002. The role of bedrock topography on subsurface storm flow. Water Resour. Res. 38, 1269.
Fu, Z.Y., Chen, H.S., Xu, Q.X., Jia, J.T., Wang, S., Wang, K.L., 2015w. Role of epikarst in near-surface hydrological processes in a soil mantled subtropical dolomite karst slope:

implications of field rainfall simulation experiments. Hydrol. Process. http://dx.doi.org/10.1002/hyp.10650 (under review).
Graham, C.B., Woods, R.A., McDonnell, J.J., 2010. Hillslope threshold response to rainfall: (1) a field based forensic approach. J. Hydrol. 393, 65–76.
Guebert, M.D., Gardner, T.W., 2001. Macropore flow on a reclaimed surface mine: infiltration and hillslope hydrology. Geomorphology 39, 151–169.
Gwenzi, W., Hinz, C., Holmes, K., Phillips, I.R., Mullins, I.J., 2011. Field-scale spatial variability of saturated hydraulic conductivity on a recently constructed artificial ecosystem. Geoderma 166, 43–56.
Heilman, J.L., Litvak, M.E., McInnes, K.J., Kjelgaard, J.F., Kamps, R.H., Schwinning, S., 2014. Water-storage capacity controls energy partitioning and water use in karst ecosystems on the Edwards Plateau, Texas. Ecohydrology 7, 127–138.
Hopp, L., McDonnell, J.J., 2009. Connectivity at the hillslope scale: identifying interactions between storm size, bedrock permeability, slope angle and soil depth. J. Hydrol. 376, 378–391.
Huang, W., Deng, C.B., Day, M.J., 2014. Differentiating tower karst (fenglin) and cockpit karst (fengcong) using DEM contour, slope, and centroid. Environ. Earth Sci. 72, 407–416.
Iserloh, T., Ries, J.B., Cerdà, A., Echeverría, M.T., Fister, W., Geißler, C., Kuhn, N.J., León, F.J., Peters, P., Schindewolf, M., Schmidt, J., Scholten, T., Seeger, M., 2012. Comparative measurements with seven rainfall simulators on uniform bare fallow land. Z. Geomorphol. 57, 11–26.
Iserloh, T., Ries, J.B., Arnaez, J., Boix Fayos, C., Butzen, V., Cerdà, A., Echeverría, M.T., Fernández-Gálvez, J., Fister, W., Geißler, C., Gómez, J.A., Gómez-Macpherson, H., Kuhn, N.J., Lázaro, R., León, F.J., Martínez-Mena, M., Martínez-Murillo, J.F., Marzen, M., Mingorance, M.D., Ortigosa, L., Peters, P., Regüés, D., Ruiz-Sinoga, J.D., Scholten, T., Seeger, M., Solé-Benet, A., Wengel, R., Wirtz, S., 2013. European small portable rainfall simulators: a comparison of rainfall characteristics. Catena 110, 100–112.
Jiang, G.H., Guo, F., Polk, J.S., Kang, Z.Q., Wu, J.C., 2015. Delineating vulnerability of karst aquifers using hydrochemical tracers in Southwestern China. Environ. Earth Sci. 74, 1015–1027.
Kirkby, M.J., 1978. Hillslope Hydrology. John Wiley and Sons Inc., New York, p. 389.
Klimchouk, A., 2004. Towards defining, delimiting and classifying epikarst: its origin, processes and variants of geomorphic evolution. Speleogenesis Evol. Karst Aquifers 2, 1–13.
Lange, J., Greenbaum, N., Husary, S., Ghanem, M., Leibundgut, C., Schick, A.P., 2003. Runoff generation from successive simulated rainfalls on a rocky, semi-arid, Mediterranean hillslope. Hydrol. Process. 17, 279–296.
Lanni, C., McDonnell, J., Hopp, L., Rigon, R., 2013. Simulated effect of soil depth and bedrock topography on near-surface hydrologic response and slope stability. Earth Surf. Process. Landf. 38, 146–159.
Leh, M.D., Chaubey, I., Murdoch, J., Brahana, J.V., Haggard, B.E., 2008. Delineating runoff processes and critical runoff source areas in a pasture hillslope of the Ozark Highlands. Hydrol. Process. 22, 4190–4204.
Li, X.Y., Contreras, S., Solé-Benet, A., Cantón, Y., Domingo, F., Lázaro, R., Lin, H., Van Wesemael, B., Puigdefábregas, J., 2011. Controls of infiltration-runoff processes in Mediterranean karst rangelands in SE Spain. Catena 86, 98–109.
Lin, H., 2010. Linking principles of soil formation and flow regimes. J. Hydrol. 393, 3–19.
Lin, H., Bouma, J., Wilding, L., Richardson, J., Kutilek, M., Nielsen, D., 2005. Advances in hydropedology. Adv. Agron. 85, 1–89.
Liu, G.S., Jiang, N.H., Zhang, L.D., Liu, Z.L., 1996. Soil physical and chemical analysis and description of soil profiles. In: Sun, H.L., Liu, G.S. (Eds.), Standard Methods for Observation and Analysis in Chinese Ecosystem Research Network. Standards Press of China, Beijing, pp. 5–40.
Liu, M.X., Xu, X.L., Sun, A.Y., Wang, K.L., Liu, W., Zhang, X.Y., 2014. Is southwestern China experiencing more frequent precipitation extremes? Environ. Res. Lett. 9, 064002.
Luk, S., Abrahams, A.D., Parsons, A.J., 1986. A simple rainfall simulator and trickle system for hydro-geo-morphical experiments. Phys. Geogr. 7, 344–356.
Martínez-Murillo, J.F., Nadal-Romero, E., Regües, D., Cerdà, A., Poesen, J., 2013. Soil erosion and hydrology of the western Mediterranean badlands throughout rainfall simulation experiments: a review. Catena 106, 101–112.
Moreno-Ramón, H., Quizembe, S.J., Ibáñez-Asensio, S., 2014. Coffee husk mulch on soil erosion and runoff: experiences under rainfall simulation experiment. Solid Earth 5, 851–862.
Nie, Y.P., Chen, H.S., Wang, K.L., Ding, Y.L., 2014. Rooting characteristics of two widely-distributed woody plant species established in rocky karst habitats of Southwest China. Plant Ecol. 215, 1099–1109.
Nobles, M.M., Wilding, L.P., Lin, H.S., 2010. Flow pathways of bromide and Brilliant Blue FCF tracers in caliche soils. J. Hydrol. 393, 114–122.
Peng, T., Wang, S.J., 2012. Effects of land use, land cover and rainfall regimes on the surface runoff and soil loss on karst slopes in Southwest China. Catena 90, 53–62.
Schwartz, B.F., Schwinning, S., Gerard, B., Kukowski, K.R., Stinson, C.L., Dammeyer, H.C., 2013. Using hydrogeochemical and ecohydrologic responses to understand epikarst process in semi-arid systems, Edwards plateau, Texas, USA. Acta Carsologica 42, 315–325.
Statistical Package for the Social Sciences Inc., 2001. SPSS Advanced Statistics 11.0. SPSS Inc., Chicago.
Tani, M., 1997. Runoff generation processes estimated from hydrological observations on a steep forested hillslope with a thin soil layer. J. Hydrol. 200, 84–109.
Taucer, P.I., Munster, C.L., Wilcox, B.P., Shade, B., Dasgupta, S., Owens, M.K., Mohanty, B., 2005. Large plot tracing of subsurface flow in the Edwards Aquifer epikarst. Proceedings of the Tenth Multidisciplinary Conference; San Antonio, Texas; USA, pp. 24–28.
Trajkovic, S., Kolakovic, S., 2009. Evaluation of reference evapotranspiration equations under humid conditions. Water Resour. Manag. 23, 3057–3067.
Tromp-van Meerveld, H.J., McDonnell, J.J., 2006. Threshold relations in subsurface stormflow: 2. The fill and spill hypothesis. Water Resour. Res. 42, W02411.
Tromp-van Meerveld, H.J., Peters, N.E., McDonnell, J.J., 2007. Effect of bedrock permeability on subsurface stormflow and the water balance of a trenched hillslope at the Panola Mountain Research Watershed, Georgia, USA. Hydrol. Process. 21, 750–769.
Weiler, M., McDonnell, J.J., Tromp-van Meerveld, H.J., Uchida, T., 2005. Subsurface stormflow. In: Anderson, M.G., McDonnell, J.J. (Eds.), Encyclopedia of Hydrological Sciences vol. 3. Wiley, Chichester, pp. 1719–1732.
Wilcox, B.P., Wilding, L.P., Woodruff Jr., C.M., 2007. Soil and topographic controls on runoff generation from stepped landforms in the Edwards Plateau of Central Texas. Geophys. Res. Lett. 34, L24S24.
Wilcox, B.P., Taucer, P.I., Munster, C.L., Owens, M.K., Mohanty, B.P., Sorenson, J.R., Bazan, R., 2008. Subsurface stormflow is important in semiarid karst shrublands. Geophys. Res. Lett. 35, L10403.
Williams, P.W., 2008. The role of the epikarst in karst and cave hydrogeology: a review. Int. J. Speleol. 37, 1–10.
Xu, E.Q., Zhang, H.Q., 2014. Characterization and interaction of driving factors in karst rocky desertification: a case study from Changshun, China. Solid Earth 5, 1329–1340.
Xu, E.Q., Zhang, H.Q., Li, M.X., 2015. Object-based mapping of karst rocky desertification using a support vector machine. Land Degrad. Dev. 26, 158–167.
Yan, X., Cai, Y.L., 2015. Multi-scale anthropogenic driving forces of karst rocky desertification in Southwest China. Land Degrad. Dev. 26, 193–200.
Yuan, D.X., 1994. Chinese Karstology. Geology Press, Beijing, pp. 1–200.
Zhang, Z.C., Chen, X., Ghadouani, A., Shi, P., 2011. Modelling hydrological processes influenced by soil, rock and vegetation in a small karst basin of Southwest China. Hydrol. Process. 25, 2456–2470.
Zhou, W.F., Beck, B.F., 2011. Engineering issues on karst. In: van Beynen, P.E. (Ed.), Karst Management. Springer, Netherlands, pp. 9–45.
Ziadat, F.M., Taimeh, A.Y., 2013. Effect of rainfall intensity, slope and land use and antecedent soil moisture on soil erosion in an arid environment. Land Degrad. Dev. 24, 582–590.